

1 **Tropopause Evolution in a Rapidly Intensifying Tropical Cyclone: A Static**
2 **Stability Budget Analysis in an Idealized, Axisymmetric Framework**

3 Patrick Duran* and John Molinari

4 *University at Albany, State University of New York, Albany, NY*

5 **Corresponding author address:* Department of Atmospheric and Environmental Sciences, Univer-
6 sity at Albany, State University of New York, 1400 Washington Avenue, Albany, NY.

7 E-mail: pduran2008@gmail.com

ABSTRACT

8 Large changes in tropopause-layer static stability are observed during the
9 rapid intensification (RI) of an idealized, axisymmetric tropical cyclone (TC).
10 Over the eye, static stability near the tropopause decreases and the cold-point
11 tropopause height rises by up to 4 km at the storm center. Outside of the eye,
12 static stability increases considerably just above the cold-point tropopause,
13 and the tropopause remains near its initial level.

14 A budget analysis reveals that advection contributes to the static stability
15 tendencies at all times throughout the upper troposphere and lower strato-
16 sphere. Differential advection is particularly important within the eye, where
17 it acts to destabilize the layer near and above the cold-point tropopause.
18 Outside of the eye, a radial-vertical circulation develops during RI, with
19 strong outflow below the tropopause and weak inflow above. Vertical wind
20 shear above and below the upper-tropospheric outflow maximum induces tur-
21 bulence, which provides forcing for both destabilization and stabilization
22 in the tropopause layer. Meanwhile, as organized convection reaches the
23 tropopause, radiative heating tendencies at the top of the cirrus canopy gen-
24 erally act to destabilize the upper troposphere and stabilize the lower strato-
25 sphere. Turbulent mixing and radiative heating combine to play an important
26 role in the development of the strong stable layer immediately above the cold-
27 point tropopause during RI. The results suggest that turbulence and radiation,
28 alongside advection, play fundamental roles in the upper-level static stability
29 evolution of TCs.

30 **1. Introduction**

31 After undergoing a remarkably rapid intensification (RI), Hurricane Patricia (2015) set a new
32 record as the strongest tropical cyclone (TC) ever observed in the Western Hemisphere (Kim-
33 berlain et al. 2016; Rogers et al. 2017). High-altitude dropsonde observations taken during the
34 Tropical Cyclone Intensity (TCI) experiment captured this RI in unprecedented detail (Doyle et al.
35 2017). These observations revealed dramatic changes in the structure of the cold-point tropopause
36 and upper-level static stability as the storm intensified (Duran and Molinari 2018).

37 At tropical storm intensity, shortly before RI commenced, a strong inversion layer existed just
38 above the cold-point tropopause. During the first half of the RI period, this inversion layer weak-
39 ened throughout Patricia’s inner core, with the weakening most pronounced over the developing
40 eye. By the time the storm reached its maximum intensity of 95 m s^{-1} , the inversion layer over
41 the eye had disappeared almost completely, which was accompanied by a greater than 1-km in-
42 crease in the tropopause height. Meanwhile over the eyewall region, the static stability increased
43 and the tropopause remained near its initial level. The mechanisms that might have led to this
44 tropopause-layer variability will be investigated in the current paper using idealized simulations.

45 Despite the importance of tropopause-layer thermodynamics in theoretical models of hurri-
46 canes (Emanuel and Rotunno 2011; Emanuel 2012), most observational studies of the upper-
47 tropospheric structure of TCs are decades old. Recently, however, Komaromi and Doyle (2017)
48 found that stronger TCs tended to have a higher and warmer tropopause over their inner core than
49 weaker TCs. Their results are consistent with the evolution observed over the inner core of Hur-
50 ricane Patricia, in which the tropopause height increased and the tropopause temperature warmed
51 throughout RI (Duran and Molinari 2018).

52 Idealized simulations of a TC analyzed by Ohno and Satoh (2015) suggested that the develop-
53 ment of an upper-level warm core near the 13-km level acted to decrease the static stability near the
54 tropopause within the eye (compare their Figs. 9,10). Although the mechanisms that might drive
55 this static stability evolution have not been examined explicitly, Stern and Zhang (2013) described
56 the development of the TC warm core using a potential temperature (θ) budget analysis. They
57 found that radial and vertical advection both played important roles in warm core development
58 throughout RI, and subgrid-scale diffusion became particularly important during the later stage of
59 RI. To our knowledge, the only paper that has examined explicitly the static stability evolution in
60 a modeled TC is Kepert et al. (2016), but their analysis was limited to the boundary layer. The
61 analysis herein is based upon that of Stern and Zhang (2013), except using a static stability budget
62 similar to that of Kepert et al. (2016), with a focus on the upper troposphere and lower stratosphere.

63 **2. Model Setup**

64 The numerical simulations were performed using version 19.4 of Cloud Model 1 (CM1) de-
65 scribed in Bryan and Rotunno (2009). The equations of motion were integrated on a 3000-km-
66 wide, 30-km-deep axisymmetric grid with 1-km horizontal and 250-m vertical grid spacing. The
67 computations were performed on an f -plane at 15°N latitude, over a sea surface with constant
68 temperature of 30.5°C, which matches that observed near Hurricane Patricia (2015; Kimberlain
69 et al. 2016). Horizontal turbulence was parameterized using the Smagorinsky scheme described
70 in Bryan and Rotunno (2009, pg. 1773), with a prescribed mixing length that varied linearly from
71 100 m at a surface pressure of 1015 hPa to 1000 m at a surface pressure of 900 hPa. Vertical
72 turbulence was parameterized using the formulation of Markowski and Bryan (2016, their Eq. 6),
73 using an asymptotic vertical mixing length of 100 m. A Rayleigh damping layer was applied out-
74 side of the 2900-km radius and above the 25-km level to prevent spurious gravity wave reflection

at the model boundaries. Microphysical processes were parameterized using the Thompson et al. (2004) scheme and radiative heating tendencies were computed every two minutes using the Rapid Radiative Transfer Model for GCMs (RRTMG) longwave and shortwave schemes (Iacono et al. 2008). The initial temperature and humidity field was horizontally homogeneous and determined by averaging all Climate Forecast System Reanalysis (CFSR) grid points within 100 km of Patricia's center of circulation at 18 UTC 21 October 2015. The vortex described in Rotunno and Emanuel (1987, their Eq. 37) was used to initialize the wind field, setting all parameters equal to the values used therein.

Although hurricanes simulated in an axisymmetric framework tend to be more intense than those observed in nature, the intensity evolution of this simulation matches reasonably well with that observed in Hurricane Patricia. After an initial spin-up period of about 20 hours, the modeled storm (Fig.1, blue lines) began an RI period that lasted approximately 30 hours. After this RI, the storm continued to intensify more slowly until the maximum 10-m wind speed reached 89 m s^{-1} and the minimum sea-level pressure reached its minimum of 846 mb, 81 hours into the simulation. Hurricane Patricia (red stars) exhibited a similar intensity evolution prior to its landfall, with an RI period leading to a maximum 10-m wind speed of 95 m s^{-1} and a minimum sea-level pressure of 872 hPa.

3. Budget Computation

The static stability can be expressed as the squared Brunt-Väisälä frequency:

$$N_m^2 = \frac{g}{T} \left(\frac{\partial T}{\partial z} + \Gamma_m \right) \left(1 + \frac{T}{R_d/R_v + q_s} \frac{\partial q_s}{\partial T} \right) - \frac{g}{1 + q_t} \frac{\partial q_t}{\partial z}, \quad (1)$$

where g is gravitational acceleration, T is temperature, R_d and R_v are the gas constants of dry air and water vapor, respectively, q_s is the saturation mixing ratio, q_t is the total condensate mixing

ratio, and Γ_m is the moist-adiabatic lapse rate:

$$\Gamma_m = g(1 + q_t) \left(\frac{1 + L_v q_s / R_d T}{c_{pm} + L_v \partial q_s / \partial T} \right), \quad (2)$$

where L_v is the latent heat of vaporization and c_{pm} is the specific heat of moist air at constant pressure. In the tropopause layer, q_s , $\partial q_s / \partial T$, and $\partial q_t / \partial z$ approach zero. In this limiting case, Eq. 1 reduces to:

$$N^2 = \frac{g}{\theta} \frac{\partial \theta}{\partial z}, \quad (3)$$

where θ is the potential temperature.

To compute N^2 , CM1 uses Eq. 1 in saturated environments and Eq. 3 in sub-saturated environments. For simplicity, however, only Eq. 3 will be employed for the budget computations¹.

Taking the time derivative of Eq. 3 yields the static stability tendency:

$$\frac{\partial N^2}{\partial t} = \frac{g}{\theta} \frac{\partial}{\partial z} \frac{\partial \theta}{\partial t} - \frac{g}{\theta^2} \frac{\partial \theta}{\partial z} \frac{\partial \theta}{\partial t}, \quad (4)$$

where the potential temperature tendency, $\partial \theta / \partial t$, can be written:

$$\frac{\partial \theta}{\partial t} = HADV + VADV + HTURB + VTURB + MP + RAD + DISS \quad (5)$$

Each term on the right-hand side of Eq. 5 represents a θ budget variable, each of which is output directly by the model every minute. HADV and VADV are the radial and vertical advective tendencies², HTURB and VTURB are the tendencies from the horizontal and vertical turbulence parameterizations, MP is the tendency from the microphysics scheme, RAD is the tendency from the radiation scheme, and DISS is the tendency due to turbulent dissipation. This equation neglects Rayleigh damping, since the entire analysis domain is outside of the regions where damping is applied. Each term in Eq. 5 is substituted for $\partial \theta / \partial t$ in Eq. 4, yielding the contribution of each

¹The validity of this approximation will be substantiated later in this section.

²These terms include the tendencies due to implicit diffusion in the fifth-order finite differencing scheme, which are output separately from the advection terms in CM1.

112 budget term to the static stability tendency. These terms are summed, yielding an instantaneous
 113 "budget change" in N^2 every minute. The budget changes are then averaged over 24-hour periods
 114 and compared to the total model change in N^2 over that same time period, i.e.:

$$\Delta N_{budget}^2 = \frac{1}{\delta t} \sum_{t=t_0}^{t_0+\delta t} \left. \frac{\partial N^2}{\partial t} \right|_t \quad (6)$$

$$\Delta N_{model}^2 = N_{t_0+\delta t}^2 - N_{t_0}^2 \quad (7)$$

$$Residual = \Delta N_{model}^2 - \Delta N_{budget}^2 \quad (8)$$

117 where t_0 is an initial time and δt is 24 hours.

118 Eqs. 6-8 are plotted for three consecutive 24-hour periods in Fig. 2. For this and all subsequent
 119 radial-vertical cross sections, a 1-2-1 smoother is applied once in the radial direction to eliminate
 120 $2\Delta r$ noise that appears in some of the raw model output and calculated fields. The left column
 121 of Fig. 2 depicts the model changes computed using Eq. 7, along with Eq. 1 in saturated envi-
 122 ronments and Eq. 3 in subsaturated environments. The center column depicts the budget changes
 123 computed using Eq. 6 along with Eq. 3 throughout the domain. Thus, the left column includes
 124 the effect of moisture in the N^2 computations, whereas the center column neglects moisture. The
 125 right column depicts the residuals, computed using Eq. 8 (i.e. the left column minus the center
 126 column.) In every 24-hour period, the budget changes are nearly identical to the model changes,
 127 which is reflected in the near-zero residuals in the right column. This indicates that the budget ac-
 128 curately represents the model variability, which implies that the neglect of moisture in the budget
 129 computation introduces negligible error within the analysis domain³.

130 In the tropopause layer, some of the budget terms are small enough to be ignored. To determine
 131 which of the budget terms are most important, a time series of the contribution of each of the

³This is not the case in the lower- and mid-troposphere, where the residual actually exceeds the budget tendencies in many places, likely due to the neglect of moisture; thus we limit this analysis to the upper troposphere and lower stratosphere.

budget terms in Eq. 5 to the tropopause-layer static stability tendency is plotted in Fig. 4. For this figure, each of the budget terms is computed using the method described in Section 3, except with 1-hour averaging intervals instead of 24-hour intervals. The absolute values of these tendencies are then averaged over the radius-height domain of the plots shown in Fig. 2 and plotted as a time series⁴. Advection (Fig. 4, red line) plays an important role in the mean tropopause-layer static stability tendency at all times, and vertical turbulence (Fig. 4, blue line) and radiation (Fig. 4, dark green line) also contribute significantly. The remaining three processes - horizontal turbulence, microphysics, and dissipative heating - lie atop one another near zero. Although the horizontal turbulence and microphysics terms can be quite large in the eyewall region, they are negligible everywhere outside of the eyewall, and do not play important roles in the mesoscale tropopause variability. Dissipative heating, meanwhile, is relatively small everywhere.

The preceding analysis indicates that, at all times, three budget terms dominate the tropopause-layer static stability tendency: advection, vertical turbulence, and radiation. Variations in the magnitude and spatial structure of these terms drive the static stability changes depicted in Fig. 2; subsequent sections will focus on these variations and what causes them.

4. Results

a. Static stability evolution

The average N^2 over the first day of the simulation (Fig. 3a) indicates the presence of a weak N^2 maximum just above the cold-point tropopause. Over the subsequent 24 hours, during the RI period, the N^2 within and above this layer decreased near the storm center (Fig. 3b). This decreasing

⁴It will be seen in subsequent figures that each of the terms contributes both positively and negatively to the N^2 tendency within the analysis domain. Thus, taking an average over the domain tends to wash out the positive and negative contributions. To circumvent this problem, the absolute value of each of the terms is averaged.

N^2 corresponded to an increase in the tropopause height within the developing eye, maximized at the storm center. Outside of the eye, meanwhile, the tropopause height decreased over the eyewall region (25-60-km radius) and increased only slightly outside of the 60-km radius. In this outer region, the N^2 maximum just above the tropopause strengthened during RI. These trends continued as the storm's intensity leveled off in the 48-72-hour period (Fig. 3c). The tropopause height increased to nearly 21 km at the storm center and sloped sharply downward to 16.3 km on the inner edge of the eyewall, near the 30 km radius. Static stability outside of the eye, meanwhile, continued to increase just above the cold-point tropopause. This N^2 evolution closely follows that observed in Hurricane Patricia (2015; Duran and Molinari 2018). The mechanisms that led to these N^2 changes will be investigated in the subsequent sections.

b. Static stability budget analysis

(i) 0-24 hours The weakening of the lower-stratospheric N^2 maximum during the initial spin-up period is reflected in the total N^2 budget change over this time (Fig. 5a). The 17-18-km layer was characterized by decreasing N^2 (purple shading), maximizing at the storm center. The layer immediately below the tropopause, meanwhile, saw increasing N^2 during this time period. Although these tendencies extended out to the 200-km radius, they were particularly pronounced at innermost radii. A comparison of the contributions of advection (Fig. 5b), vertical turbulence (Fig. 5c), and radiation (Fig. 5d) reveals that advection was the primary drive of the N^2 tendency during this period. Although vertical turbulence acted in opposition to advection (i.e. it acted to stabilize regions that advection acted to destabilize), the magnitude of the advective tendencies was larger, particularly at the innermost radii. The sum of advection and vertical turbulence (Fig. 5e) almost exactly replicated the static stability tendencies above 17 km. Radiative tendencies, meanwhile, (Fig. 5d) acted to destabilize the layer below about 16 km and stabilize the layer between 16 and

175 17 km. The sum of advection, vertical turbulence, and radiation (Fig. 5f) reproduces the total
176 change in N^2 almost exactly.

177 (ii) *24-48 hours* During the RI period, N^2 within the eye generally decreased above 16 km and
178 increased below (Fig. 6a). These tendencies at the innermost radii were driven almost entirely by
179 advection (Fig. 6b); vertical turbulence (Fig. 6c) and radiation (Fig. 6d) contributed negligibly to
180 the static stability tendencies in this region.

181 Outside of the eye, the N^2 evolution exhibited alternating layers of positive and negative tenden-
182 cies. Near and above 18 km existed an upward-sloping region of decreasing N^2 that extended out
183 to the 180-km radius. In this region, neither vertical turbulence nor radiation exhibited negative
184 N^2 tendencies; advection was the only forcing for destabilization. Immediately below this layer
185 was a region of increasing N^2 , which sloped upward from 17 km near the 30-km radius to just
186 below 18 km outside of the 100-km radius. Advection and vertical turbulence both contributed to
187 this positive N^2 tendency, with advection playing an important role below about 17.5 km and and
188 turbulence playing an important role above. The sum of advection and turbulence (Fig. 6e) reveals
189 two discontinuous regions of increasing N^2 in the 17-18-km layer rather than one contiguous re-
190 gion. The addition of radiation to these two terms, however, (Fig. 6f) provides the link between
191 these two regions, indicating that radiation also plays a role in strengthening the stable layer just
192 above the tropopause. In the 16-17-km layer, a horizontally-extensive layer of decreasing N^2 also
193 was forced by a combination of advection, vertical turbulence, and radiation. The sum of advec-
194 tion and vertical turbulence accounts for only a portion of the decreasing N^2 in this layer, and
195 actually indicates forcing for stabilization near the 50-km radius and outside of the 130-km radius.
196 Radiative tendencies overcome this forcing for stabilization in both of these regions to produce the
197 radially-extensive region of destabilization observed just below the tropopause.

198 The sum of advection, vertical turbulence, and radiation (Fig. 6f) once again closely follows
199 the observed N^2 variability, except lower in the eyewall where the neglect of latent heating and
200 horizontal turbulence introduces some differences.

201 (iii) 48-72 hours After the storm's maximum wind speed leveled off near 80 m s^{-1} , the magnitude
202 of the static stability tendencies within the eye decreased to near zero (Fig. 7a).

203 Outside of the eye, however, N^2 continued to increase just above the tropopause and decrease
204 just below. The sum of advection and vertical turbulence (Fig. 7e) indicates that the increase of
205 N^2 observed in the 17-18-km layer and inside of the 80-km radius cannot be attributed to these
206 processes, since the sum of these two terms provided forcing for destabilization. Instead, radia-
207 tion (Fig. 7d), provided the forcing for stabilization in this region. Outside of the 80-km radius,
208 both advection (Fig. 7b) and vertical turbulence (Fig. 7c) provided forcing for stabilization near
209 the 18-km level. The sum of the two terms (Fig. 7e) indicates increasing N^2 near the 18-km level
210 everywhere outside of the 80-km radius, but this stabilization is slightly weaker in the 90-120-km
211 radial band than the observed value. The addition of radiation (Fig. 7f) provides the extra forc-
212 ing for stabilization required to account for the observed increase in N^2 . Outside of the 120-km
213 radius, the region of radiative forcing for stabilization slopes downward, and the increase in N^2
214 observed near 18 km can be explained entirely by a combination of advection and vertical turbu-
215 lence. The layer of decreasing N^2 observed near 17 km was forced primarily by vertical turbulence
216 and radiation. Within most of this region, advection provided strong forcing for stabilization, but
217 this forcing was outweighed by the negative N^2 tendencies induced by a combination of vertical
218 turbulence and radiation.

219 5. Discussion

220 *a. The role of advection*

221 Advection played an important role in the tropopause-layer N^2 evolution at all stages of intensi-
222 fication, but for brevity, this section will focus only on the RI (24-48-hour) period. To investigate
223 the advective processes more closely, the individual contributions of horizontal and vertical advec-
224 tion during the RI period are shown in Fig. 8, along with the corresponding time-mean radial and
225 vertical velocities and θ . The N^2 tendencies due to the two advective components (Fig. 8a,b) ex-
226 hibit strong cancellation, consistent with flow that is nearly isentropic. There are, however, many
227 regions in which flow crosses θ surfaces; this flow accounts for all non-zero N^2 tendencies due to
228 advection previously seen in Fig. 6b.

229 During the RI period, strong radial and vertical circulations developed near the tropopause
230 (Fig. 8c,d), which forced high-magnitude N^2 tendencies due to advection (Fig. 8a,b). A layer
231 of strong outflow formed at and below the tropopause during this period, with the outflow maxi-
232 mum (dashed cyan line) curving from the 14-km level at the 50-km radius to just below the 16-km
233 level outside of the 80-km radius (Fig. 8c). Notably, the N^2 tendency due to horizontal advection
234 (Fig. 8a) tended to switch signs at this line, with stabilization below the outflow maximum and
235 destabilization above. Outside of the eye and eyewall, isentropes generally sloped upward with
236 radius. Vertical wind shear acting on these upward-sloping isentropes should act to tilt them into
237 the vertical above the outflow maximum, thereby decreasing $\partial\theta/\partial z$, and tilt them to be more hor-
238 izontal below the outflow maximum, thereby increasing $\partial\theta/\partial z$. This mechanism is the same as
239 that discussed in Trier and Sharman (2009), and is consistent with the change in sign of the N^2
240 tendency at the level of maximum outflow.

241 Meanwhile in the lower stratosphere, a thin layer of 2-4 m s⁻¹ inflow developed a few hundred
242 meters above the tropopause, similar to that which was observed in Hurricane Patricia (2015;
243 Duran and Molinari 2018) and in previous modeling studies (e.g. Ohno and Satoh 2015; Kieu et al.
244 2016). Since the isentropes in this layer sloped slightly upward with radius (i.e. $\partial\theta/\partial r < 0$), this
245 inflow acted to import lower θ air from outer radii to inner radii. Since the negative θ tendencies
246 maximized at the level of maximum inflow, the layer below the inflow maximum destabilized and
247 the layer above stabilized (Fig. 8a).

248 Curiously, horizontal advection contributed to the N^2 tendency everywhere within the eye, even
249 though the mean radial velocity was near zero. Close examination of the model output revealed
250 that these tendencies were forced by advective processes associated with inward-propagating
251 waves. Although the radial velocity perturbations induced by these waves averaged out to zero, the
252 advective tendencies forced by the radial velocity perturbations did not. Additionally, when these
253 waves reached $r=0$, a dipole of vertical velocity resulted, with ascent above and descent below. For
254 reasons that remain unclear, the regions of ascent were more persistent than the regions of descent,
255 which resulted in the mean ascent observed near $r=0$ above 17 km in Fig. 8b.

256 Vertical advection also played an important role in the tropopause-layer static stability evolution.
257 Within the eye, subsidence dominated below 17 km, while mean ascent existed near the storm
258 center above 17 km. Although the magnitude of the subsidence was larger at lower altitudes,
259 $\partial\theta/\partial z$ was smaller there. Because $\partial\theta/\partial z$ was smaller, the subsidence at lower levels could not
260 accomplish as much warming as the subsidence at higher levels in the eye, consistent with the
261 results of Stern and Zhang (2013). As a result, vertical advection within the eye acted to stabilize
262 the layer below 16 km during RI.

263 Outside of the 27-km radius, ascent dominated the troposphere, while a 1.5-km-deep layer of
264 descent existed immediately above the tropopause. These regions of ascent and descent converged

265 just above the tropopause; this convergence acted to compact the isentropes in this layer and
266 increase the static stability. Above the lower-stratospheric subsidence maximum, meanwhile, ver-
267 tical advection acted to decrease N^2 . In the troposphere, differential vertical advection increased
268 N^2 within the eyewall region and above the vertical velocity maximum at larger radii. Outside
269 of the eyewall and below the vertical velocity maximum, meanwhile, vertical advection acted to
270 decrease N^2 .

271 Comparing the N^2 tendencies forced by horizontal (Fig. 8a) and vertical (Fig. 8b) advection
272 to the total advective tendency seen in Fig. 6b reveals that horizontal advective tendencies domi-
273 nated the troposphere, while vertical advective tendencies dominated the layer near and above the
274 tropopause. Thus, tilting of isentropes in the vicinity of the upper-tropospheric outflow maximum
275 appears to be the most important process governing the N^2 tendency in the troposphere, whereas
276 convergence of vertical velocity appears to be the most important process near the tropopause.

277 *b. The role of radiation*

278 During the initial spin-up period (0-24 hours; Fig. 9a), convection was not deep enough to
279 deposit large quantities of ice near the tropopause to create a persistent cirrus canopy. Due to the
280 lack of ice particles, the radiative heating tendencies during this period (Fig. 9b) were relatively
281 small and confined to the region above a few particularly strong, although transient, convective
282 towers. During RI (24-48 hours; Fig. 9b), the eyewall updraft strengthened and a radially-extensive
283 cirrus canopy developed near the tropopause. The enhanced vertical gradient of ice mixing ratio
284 at the top of the cirrus canopy induced strong diurnal-mean radiative cooling near the tropopause
285 (Fig. 9d). This cooling exceeded 0.6 K h^{-1} in some places and sloped downward from the lower
286 stratosphere into the upper troposphere, following the top of the cirrus canopy. A small radiative
287 warming maximum also appeared outside of the 140-km radius below this region of cooling. These

288 results broadly agree with those of Bu et al. (2014; see their Fig. 11a), whose CM1 simulations
289 produced a 0.3 K h^{-1} diurnally-averaged radiative cooling at the top of the cirrus canopy and
290 radiative warming within the cloud that maximized near the 200-km radius. This broad region
291 of radiative cooling acted to destabilize the layer below the cooling maximum and stabilize the
292 layer above, which can be seen in Fig. 6d. The small area of net radiative heating outside of the
293 140-km radius enhanced the destabilization above 16 km in this region and produced a thin layer
294 of stabilization in the 15-16-km layer.

295 After the TC's RI period completed (48-72 hours; Fig. 9f), strong radiative cooling remained
296 near the tropopause at inner radii, sloping downward with the top of the cirrus canopy to below
297 the tropopause at outer radii. Cooling rates exceeded 1 K h^{-1} just above the tropopause between
298 the 30- and 70-km radii. This value is more than three times the maximum cooling rate of 0.3 K h^{-1}
299 observed by Bu et al. (2014), a discrepancy that is a consequence of their larger vertical grid
300 spacing compared to that used here, along with a contribution from differing radiation schemes.
301 To compare our results to those of Bu et al. (2014), we ran a simulation identical to that described
302 in Section 2, except using the NASA-Goddard radiation scheme and 625-m vertical grid spacing,
303 to match those of Bu et al. (2014). This simulation produced a maximum radiative cooling rate
304 of 0.3 K h^{-1} , which agrees with that shown in Bu et al. (2014). Another simulation using 625-m
305 vertical grid spacing and RRTMG radiation produced cooling rates of up to 0.6 K h^{-1} , which is
306 consistent with the WRF simulations of Bu et al. (2014). This suggests that vertical grid spacing
307 smaller than 625 m is necessary to resolve properly the radiative cooling at the top of the cirrus
308 canopy, and that the results can be quite sensitive to the radiation scheme used.

309 Time-mean radiative warming spread from 30- to 160-km radius within the cirrus canopy. The
310 existence of radiative cooling overlying radiative warming in this region led to radiatively-forced
311 destabilization at and below the tropopause, as was observed in Fig. 7d. Beneath the warming

312 layer existed a region of forcing for stabilization, while a much stronger region of forcing for
313 stabilization existed in the lower stratosphere, above the cooling maximum.

314 The results herein suggest that radiative heating tendencies played an important role in destabi-
315 lizing the upper troposphere and stabilizing the lower stratosphere after the cirrus canopy devel-
316 oped.

317 *c. The role of turbulent mixing*

318 Although vertical turbulence always acts to eliminate vertical gradients of θ , this adjustment
319 toward a neutral state only occurs where the mixing takes place. If turbulence occurs in a stably-
320 stratified layer, it will act to decrease θ at the top of the layer and increase it below. Just above and
321 just below the mixed layer, however, the θ profile remains undisturbed. Consequently, although
322 turbulent mixing acts to decrease $\partial\theta/\partial z$ in the layer in which it is occurring, it actually increases
323 $\partial\theta/\partial z$ just below and just above the layer. These vertical gradients of turbulent mixing are quite
324 important, particularly on the flanks of the upper-tropospheric outflow jet.

325 Two distinct maxima of vertical eddy diffusivity developed in the tropopause layer as the storm
326 intensified (Fig. 10). Comparison of these turbulent regions to the N^2 tendencies in Figs. 6c and
327 7c reveals that the layers in which vertical eddy diffusivity maximized corresponded to layers of
328 destabilization due to vertical turbulence. Just outside of these layers, however, vertical turbulence
329 acted to increase N^2 . The large vertical gradient of vertical eddy diffusivity near the tropopause
330 played an important role in developing the lower-stratospheric stable layer during RI. This supports
331 the hypothesized role of turbulence in setting the outflow-layer θ stratification in Rotunno and
332 Emanuel (1987).

333 6. Conclusions

334 The simulated N^2 evolution shown herein closely matched that observed during the RI of Hur-
335 ricane Patricia (2015). Three processes dominated the N^2 variability in the upper troposphere and
336 lower stratosphere: advection, radiation, and vertical turbulence. Radiation and vertical turbulence
337 played particularly important roles in developing the strong N^2 maximum just above the cold-point
338 tropopause during RI. Since these two processes are parameterized, and radiation closely depends
339 on yet another parameterized process (microphysics), the tropopause-layer N^2 variability could be
340 quite sensitive to the assumptions inherent to the parameterizations used. A better understanding
341 of the microphysical characteristics of the TC cirrus canopy, its interaction with radiation, and
342 outflow-layer turbulence is critical to understanding the tropopause-layer N^2 evolution.

343 In this paper, all of the variables were averaged over a full diurnal cycle to eliminate the effects
344 of diurnal variability and isolate the overall storm evolution. Diurnal variations in static stability
345 near the tropopause are potentially of interest with respect to the tropical cyclone diurnal cycle,
346 however, and will be the subject of future work.

347 *Acknowledgments.* We are indebted to George Bryan for his continued development and support
348 of Cloud Model 1. We also thank Jeffrey Kepert, Robert Fovell, and Erika Navarro for helpful
349 conversations related to this work. This research was supported by NSF Grant #1636799.

350 APPENDIX

351 Sensitivity experiments

352 The simulations exhibited some sensitivity to the initial thermodynamic profile and the pre-
353 scribed vertical mixing length. Although the details of the intensification and the tropopause-layer

354 N^2 evolution varied when these quantities were changed, the conclusions of the paper remain
355 unchanged.

356 *a. Sensitivity to the initial thermodynamic profile*

357 A number of sensitivity experiments were conducted using a variety of initial soundings. Chang-
358 ing the initial temperature and humidity profiles affected the timing of the onset of organized deep
359 convection and the rapidity of intensification. In all simulations, however, convection eventually
360 penetrated to the tropopause, at which time vertical turbulence and radiation combined with ad-
361 vection to adjust the N^2 profile toward that which was observed in the control run. By the end of
362 the RI period in every simulation, all three processes were actively modifying the N^2 profile near
363 the tropopause.

364 As an example, 24-hour averages of N^2 are plotted in Fig. A1 for a simulation that was identical
365 to that used in this paper, except the initial sounding was determined by averaging every CFSR
366 grid point within 1000 km of TC Patricia’s storm center at 18 UTC 21 October 2015 instead of
367 averaging only within the 100-km radius. Although the lower-stratospheric stable layer developed
368 more slowly and was weaker than that shown in Fig. 3, the overall evolution was quite similar and
369 the same budget terms dominated the N^2 evolution.

370 *b. Sensitivity to the vertical mixing length*

371 The rate of turbulent mixing in the Smagorinsky scheme used herein is highly dependent on a
372 prescribed length scale. The vertical mixing length used in this paper (100 m) was based on the
373 sensitivity experiments of Bryan (2012). Prescribing a smaller mixing length produces smaller
374 θ tendencies due to turbulence, but even with a mixing length on the low end of those tested
375 by Bryan (2012), turbulence still played an important role in the tropopause-layer N^2 evolution.

376 Fig. A2 shows the 24-hour-averaged contributions of turbulent mixing to the N^2 evolution from
377 a simulation identical to that used in this paper, except with a vertical mixing length of 50 m. At
378 all times, vertical turbulence still played an important role in the tropopause-layer N^2 evolution,
379 particularly during the latter stages of RI (48-72 hours).

380 References

- 381 Bryan, G. H., 2012: Effects of surface exchange coefficients and turbulence length scales on the
382 intensity and structure of numerically simulated hurricanes. *Mon. Wea. Rev.*, **140**, 1125–1143.
- 383 Bryan, G. H., and R. Rotunno, 2009: The maximum intensity of tropical cyclones in axisymmetric
384 numerical model simulations. *Mon. Wea. Rev.*, **137**, 1770–1789.
- 385 Bu, Y. P., R. G. Fovell, and K. L. Corbosiero, 2014: Influence of cloud-radiative forcing on tropical
386 cyclone structure. *J. Atmos. Sci.*, **71**, 1644–1622.
- 387 Doyle, J. D., and Coauthors, 2017: A view of tropical cyclones from above: The Tropical Cyclone
388 Intensity (TCI) Experiment. *Bull. Amer. Meteor. Soc.*, **98**, 2113–2134.
- 389 Duran, P., and J. Molinari, 2018: Dramatic inner-core tropopause variability during the rapid
390 intensification of Hurricane Patricia (2015). *Mon. Wea. Rev.*, **146**, 119–134.
- 391 Emanuel, K., 2012: Self-stratification of tropical cyclone outflow. Part II: Implications for storm
392 intensification. *J. Atmos. Sci.*, **69**, 988–996.
- 393 Emanuel, K., and R. Rotunno, 2011: Self-stratification of tropical cyclone outflow. Part I: Impli-
394 cations for storm structure. *J. Atmos. Sci.*, **68**, 2236–2249.

395 Iacono, M. J., J. S. Delamere, E. J. Mlawer, M. W. Shephard, S. A. Clough, and W. D. Collins,
 396 2008: Radiative forcing by long-lived greenhouse gases: Calculations with the AER radiative
 397 transfer models. *J. Geophys. Res.*, **113** (D13103).

398 Kepert, J. D., J. Schwendike, and H. Ramsay, 2016: Why is the tropical cyclone boundary layer
 399 not "well mixed"? *J. Atmos. Sci.*, **73**, 957–973.

400 Kieu, C., V. Tallapragada, D.-L. Zhang, and Z. Moon, 2016: On the development of double warm-
 401 core structures in intense tropical cyclones. *J. Atmos. Sci.*, **73**, 4487–4506.

402 Kimberlain, T. B., E. S. Blake, and J. P. Cangialosi, 2016: Tropical cyclone report: Hurricane
 403 Patricia. National Hurricane Center. [Available online at www.nhc.noaa.gov].

404 Komaromi, W. A., and J. D. Doyle, 2017: Tropical cyclone outflow and warm core structure as
 405 revealed by HS3 dropsonde data. *Mon. Wea. Rev.*, **145**, 1339–1359.

406 Markowski, P. M., and G. H. Bryan, 2016: LES of laminar flow in the PBL: A potential problem
 407 for convective storm simulations. *Mon. Wea. Rev.*, **144**, 1841–1850.

408 Ohno, T., and M. Satoh, 2015: On the warm core of a tropical cyclone formed near the tropopause.
 409 *J. Atmos. Sci.*, **72**, 551–571.

410 Rogers, R. F., S. Aberson, M. M. Bell, D. J. Cecil, J. D. Doyle, J. Morgerman, L. K. Shay, and
 411 C. Velden, 2017: Re-writing the tropical record books: The extraordinary intensification of
 412 Hurricane Patricia (2015). *Bull. Amer. Meteor. Soc.*, **98**, 2091–2112.

413 Rotunno, R., and K. A. Emanuel, 1987: An air-sea interaction theory for tropical cyclones. Part II:
 414 Evolutionary study using a nonhydrostatic axisymmetric numerical model. *J. Atmos. Sci.*, **44**,
 415 542–561.

416 Stern, D. P., and F. Zhang, 2013: How does the eye warm? Part I: A potential temperature budget
417 analysis of an idealized tropical cyclone. *J. Atmos. Sci.*, **70**, 73–89.

418 Thompson, G., R. M. Rasmussen, and K. Manning, 2004: Explicit forecasts of winter precipitation
419 using an improved bulk microphysics scheme. Part I: Description and sensitivity analysis. *Mon.*
420 *Wea. Rev.*, **132**, 519–542.

421 Trier, S. B., and R. D. Sharman, 2009: Convection-permitting simulations of the environment sup-
422 porting widespread turbulence within the upper-level outflow of a mesoscale convective system.
423 *Mon. Wea. Rev.*, **137**, 1972–1990.

424 LIST OF FIGURES

- 425 **Fig. 1.** The maximum 10-m wind speed (top panel; m s^{-1}) and minimum sea-level pressure (bottom
426 panel; hPa) in the simulated storm (blue lines; plotted every minute) and from Hurricane
427 Patricia's best track (red stars; plotted every six hours beginning at the time Patricia attained
428 tropical storm intensity). The rapid weakening during the later stage of Patricia's lifetime
429 was induced by landfall. 25
- 430 **Fig. 2.** Left panels: Twenty-four-hour changes in squared Brunt-Väisälä frequency (N^2 ; 10^{-4} s^{-2})
431 computed using Eq. 7 over (top row) 0-24 hours, (middle row) 24-48 hours, (bottom row)
432 48-72 hours. Middle Panels: The N^2 change over the same time periods computed using
433 Eqs. 4-6, Right Panels: The budget residual over the same time periods, computed by
434 subtracting the budget change (middle column) from the model change (left column). 26
- 435 **Fig. 3.** Twenty-four-hour averages of squared Brunt-Väisälä frequency (N^2 ; 10^{-4} s^{-2}) over (a) 0-24
436 hours, (b) 24-48 hours, (c) 48-72 hours. Orange lines represent the cold-point tropopause
437 averaged over the same time periods. 27
- 438 **Fig. 4.** Time series of the contribution of each of the budget terms to the time tendency of the
439 squared Brunt-Väisälä frequency (N^2 ; 10^{-4} s^{-2}). For each budget term, the absolute value
440 of the N^2 tendency is averaged temporally over 1-hour periods (using output every minute),
441 and spatially in a region extending from 0 to 200 km radius and 14 to 21 km altitude. 28
- 442 **Fig. 5.** (a) Total change in N^2 over the 0-24-hour period ($10^{-4} \text{ s}^{-2} (24 \text{ h})^{-1}$) and the contributions to
443 that change from (b) the sum of horizontal and vertical advection, (c) vertical turbulence, (d)
444 longwave and shortwave radiation, (e) the sum of horizontal advection, vertical advection,

445	and vertical turbulence, and (f) the sum of horizontal advection, vertical advection, vertical	
446	turbulence, and longwave and shortwave radiation.	30
447	Fig. 6. As in Fig. 5, but for the 24-48-hour period.	31
448	Fig. 7. As in Fig. 5, but for the 48-72-hour period.	32
449	Fig. 8. The contribution to the change in N^2 over the 24-48-hour period ($10^{-4} \text{ s}^{-2} (24 \text{ h})^{-1}$) by (a) hor-	
450	izontal advection and (b) vertical advection. (c) The radial velocity (m s^{-1} ; filled contours),	
451	potential temperature (K; thick black contours), cold-point tropopause height (orange line),	
452	and level of maximum outflow (dashed cyan line) averaged over the 24-48-hour period. (d)	
453	The vertical velocity (cm s^{-1} ; filled contours), potential temperature (K; thick black con-	
454	tours), and cold-point tropopause height (orange line) averaged over the 24-48-hour period.	
455	33	
456	Fig. 9. Ice mixing ratio (g kg^{-1}) and cold-point tropopause height (orange lines) averaged over (a)	
457	0-24 hours, (c) 24-48 hours, and (e) 48-72 hours. Radiative heating rate (K h^{-1}) and cold-	
458	point tropopause height (orange lines) averaged over (b) 0-24 hours, (d) 24-48 hours, and (f)	
459	48-72 hours.	35
460	Fig. 10. Vertical eddy diffusivity ($\text{m}^2 \text{ s}^{-2}$; filled contours), cold-point tropopause height (cyan lines),	
461	and radial velocity (m s^{-1} ; thick black lines) averaged over (a) 0-24 hours, (b) 24-48 hours,	
462	and (c) 48-72 hours.	36
463	Fig. A1. Twenty-four-hour averages of squared Brunt-Väisälä frequency (N^2 ; 10^{-4} s^{-2}) over (a) 0-24	
464	hours, (b) 24-48 hours, (c) 48-72 hours, and (d) 72-96 hours for the simulation described in	

465	Appendix Aa. Orange lines represent the cold-point tropopause averaged over the same time	
466	periods.	37
467	Fig. A2. The contribution of vertical turbulence to the N^2 variability ($10^{-4} \text{ s}^{-2} (24 \text{ h})^{-1}$) averaged over	
468	(a) 0-24 hours, (b) 24-48 hours, (c) 48-72 hours, and (d) 72-96 hours for the simulation	
469	described in Appendix Ab.	38

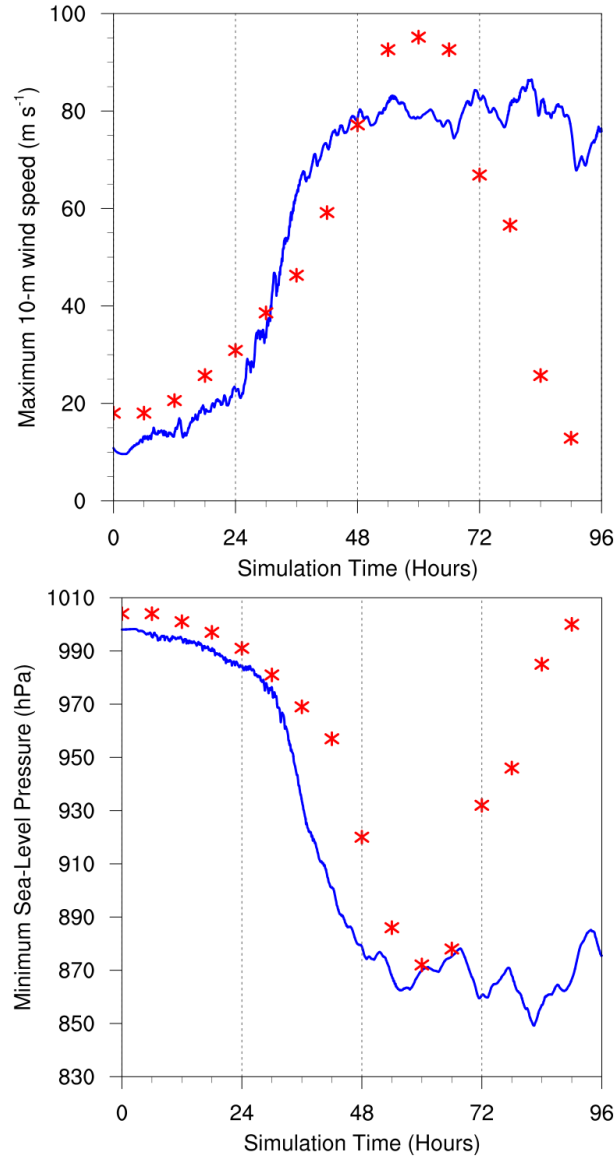
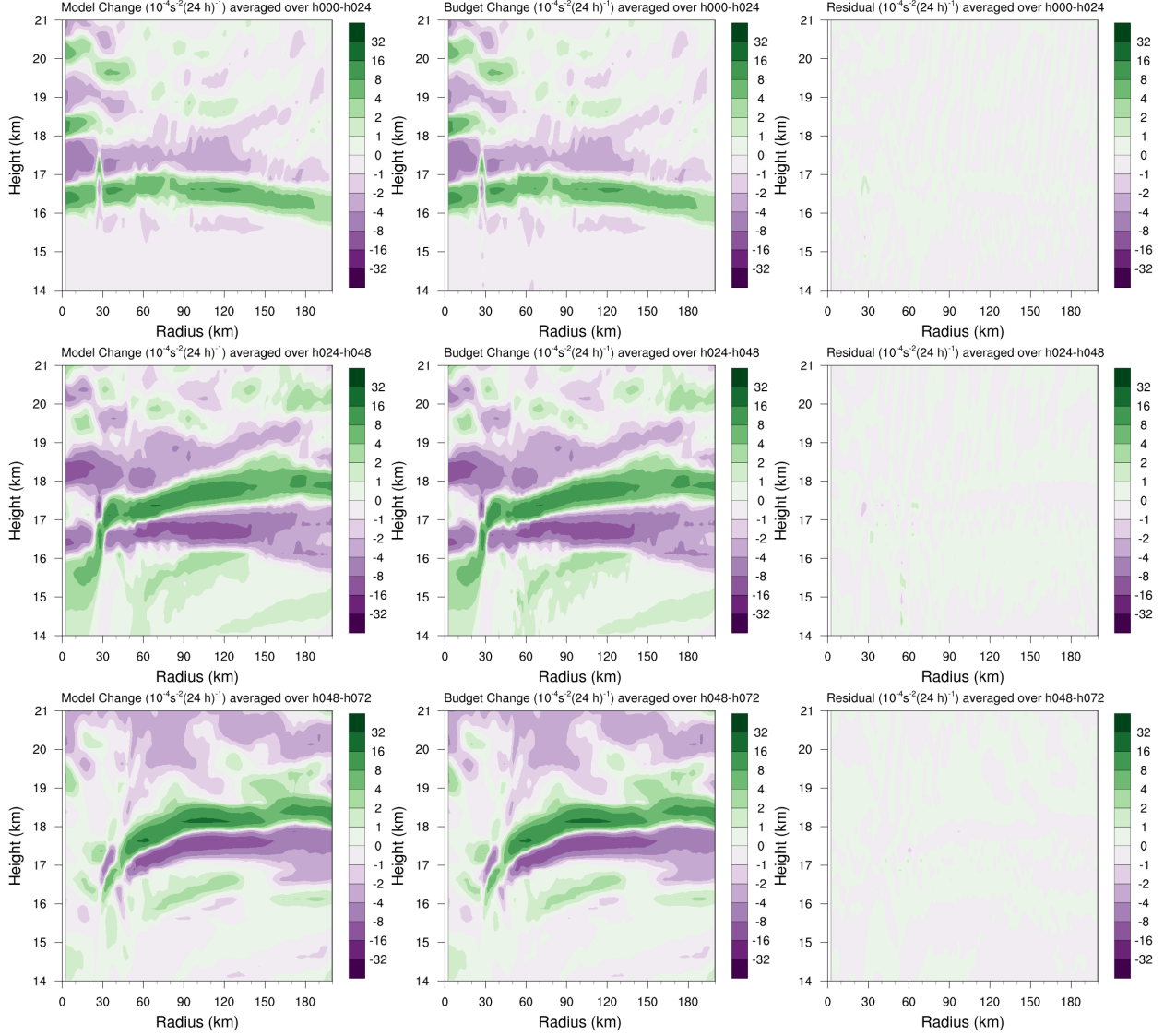


FIG. 1. The maximum 10-m wind speed (top panel; m s^{-1}) and minimum sea-level pressure (bottom panel; hPa) in the simulated storm (blue lines; plotted every minute) and from Hurricane Patricia's best track (red stars; plotted every six hours beginning at the time Patricia attained tropical storm intensity). The rapid weakening during the later stage of Patricia's lifetime was induced by landfall.



474 FIG. 2. Left panels: Twenty-four-hour changes in squared Brunt-Väisälä frequency (N^2 ; 10^{-4} s^{-2}) computed
 475 using Eq. 7 over (top row) 0-24 hours, (middle row) 24-48 hours, (bottom row) 48-72 hours. Middle Panels:
 476 The N^2 change over the same time periods computed using Eqs. 4-6, Right Panels: The budget residual over the
 477 same time periods, computed by subtracting the budget change (middle column) from the model change (left
 478 column).

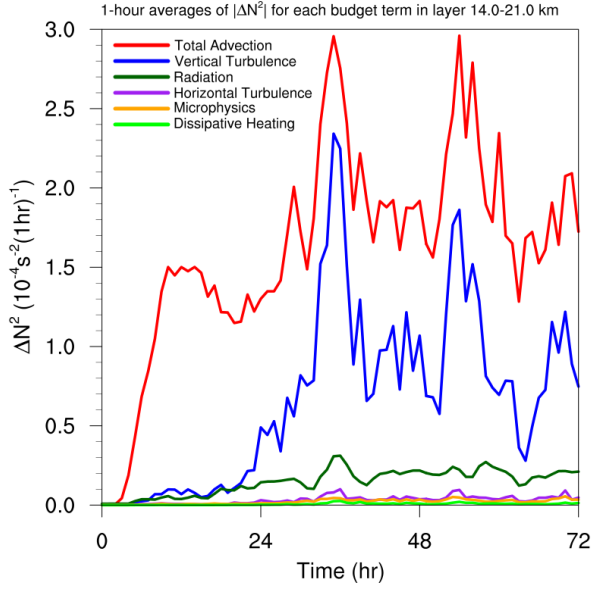


FIG. 3. Time series of the contribution of each of the budget terms to the time tendency of the squared Brunt-Väisälä frequency (N^2 ; 10^{-4} s^{-2}). For each budget term, the absolute value of the N^2 tendency is averaged temporally over 1-hour periods (using output every minute), and spatially in a region extending from 0 to 200 km radius and 14 to 21 km altitude.

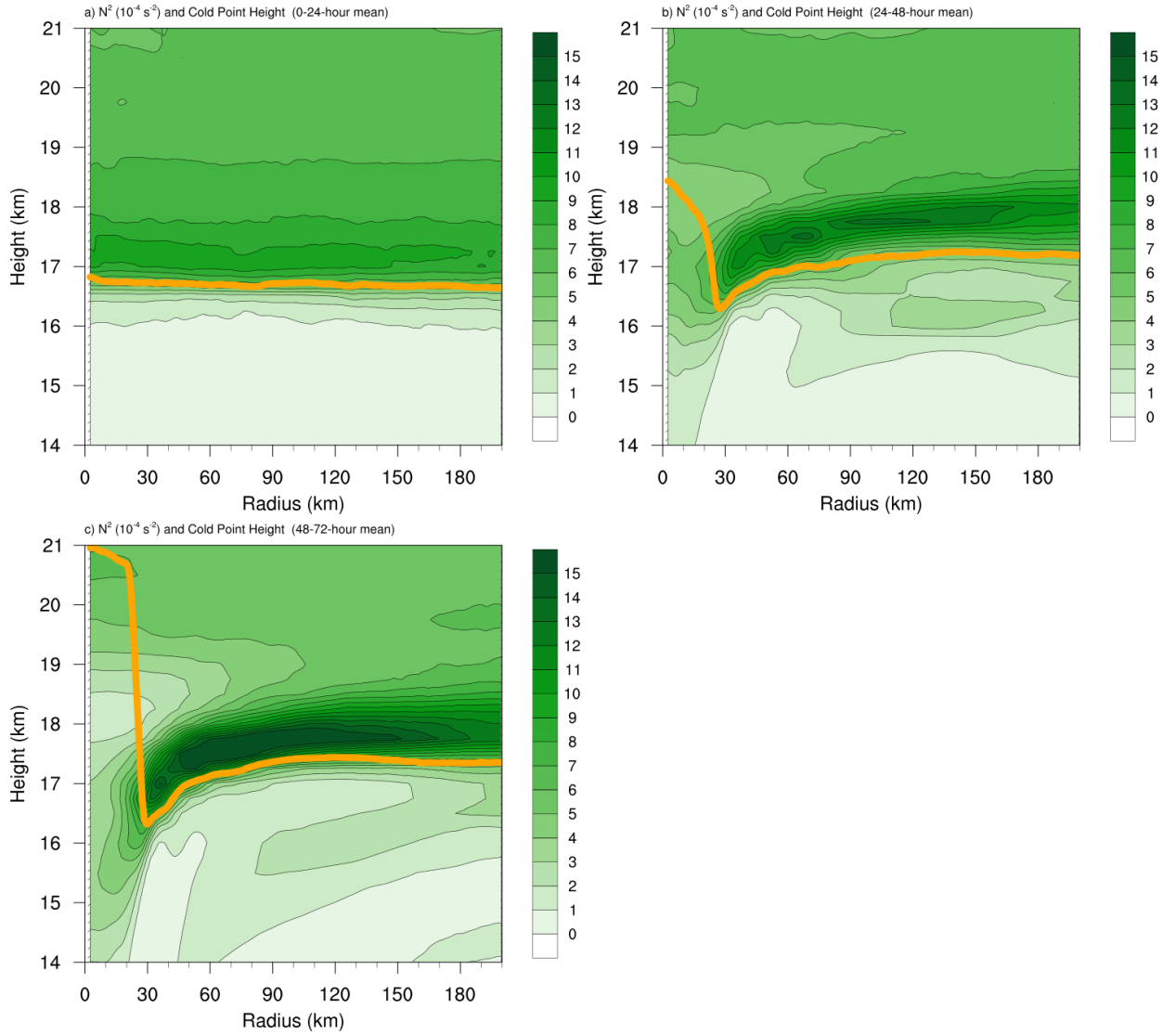
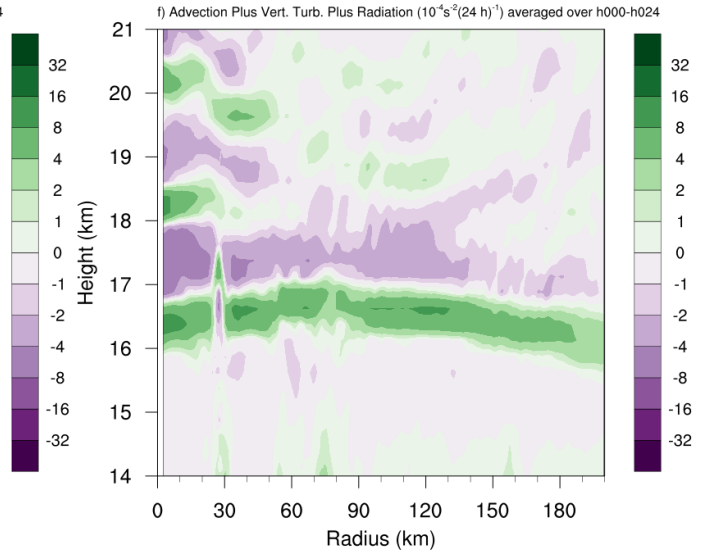
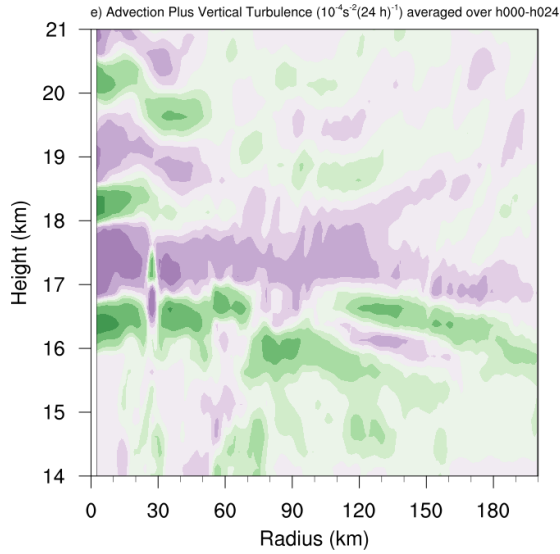
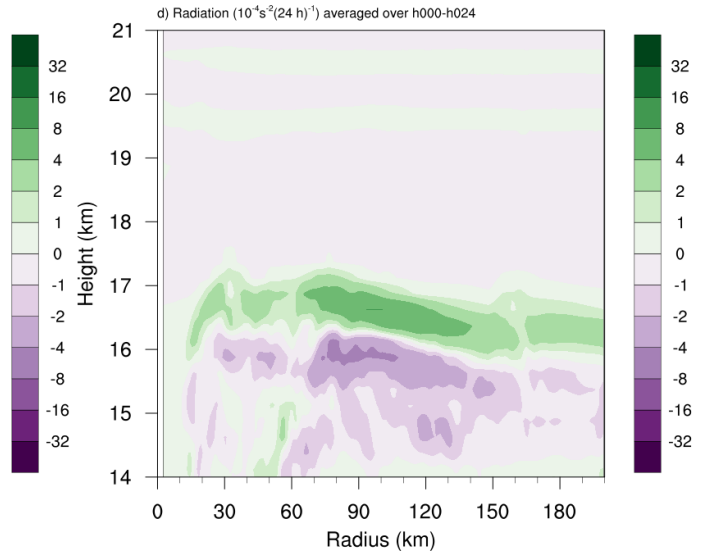
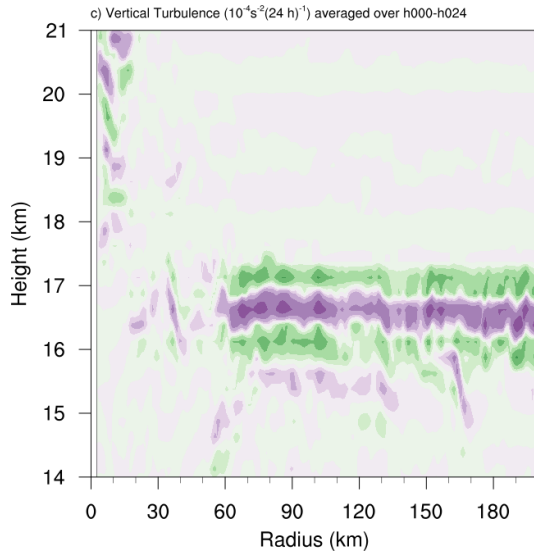
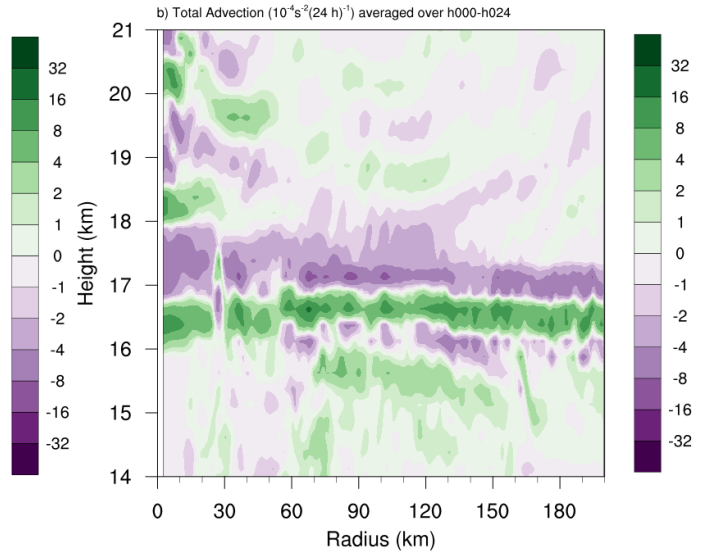
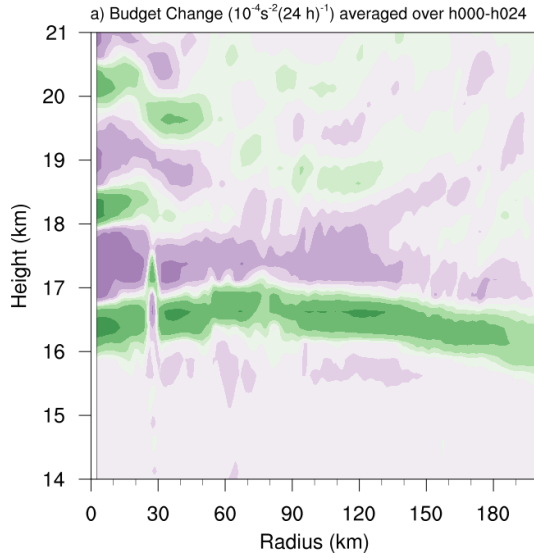


FIG. 4. Twenty-four-hour averages of squared Brunt-Väisälä frequency (N^2 ; 10^{-4} s^{-2}) over (a) 0-24 hours, (b) 24-48 hours, (c) 48-72 hours. Orange lines represent the cold-point tropopause averaged over the same time periods.



486 FIG. 5. (a) Total change in N^2 over the 0-24-hour period ($10^{-4} \text{ s}^{-2} (24 \text{ h})^{-1}$) and the contributions to that change
487 from (b) the sum of horizontal and vertical advection, (c) vertical turbulence, (d) longwave and shortwave
488 radiation, (e) the sum of horizontal advection, vertical advection, and vertical turbulence, and (f) the sum of
489 horizontal advection, vertical advection, vertical turbulence, and longwave and shortwave radiation.

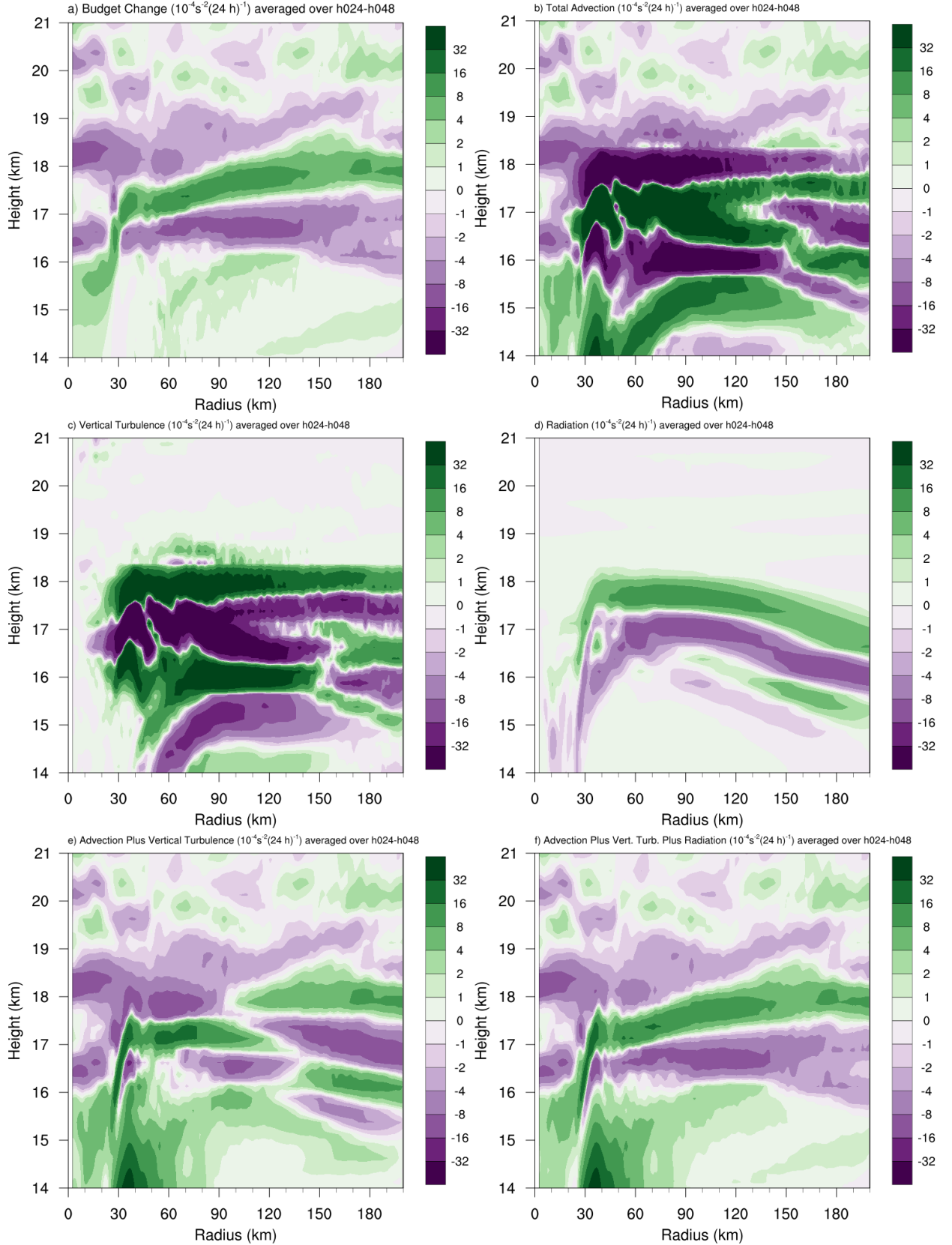


FIG. 6. As in Fig. 5, but for the 24-48-hour period.

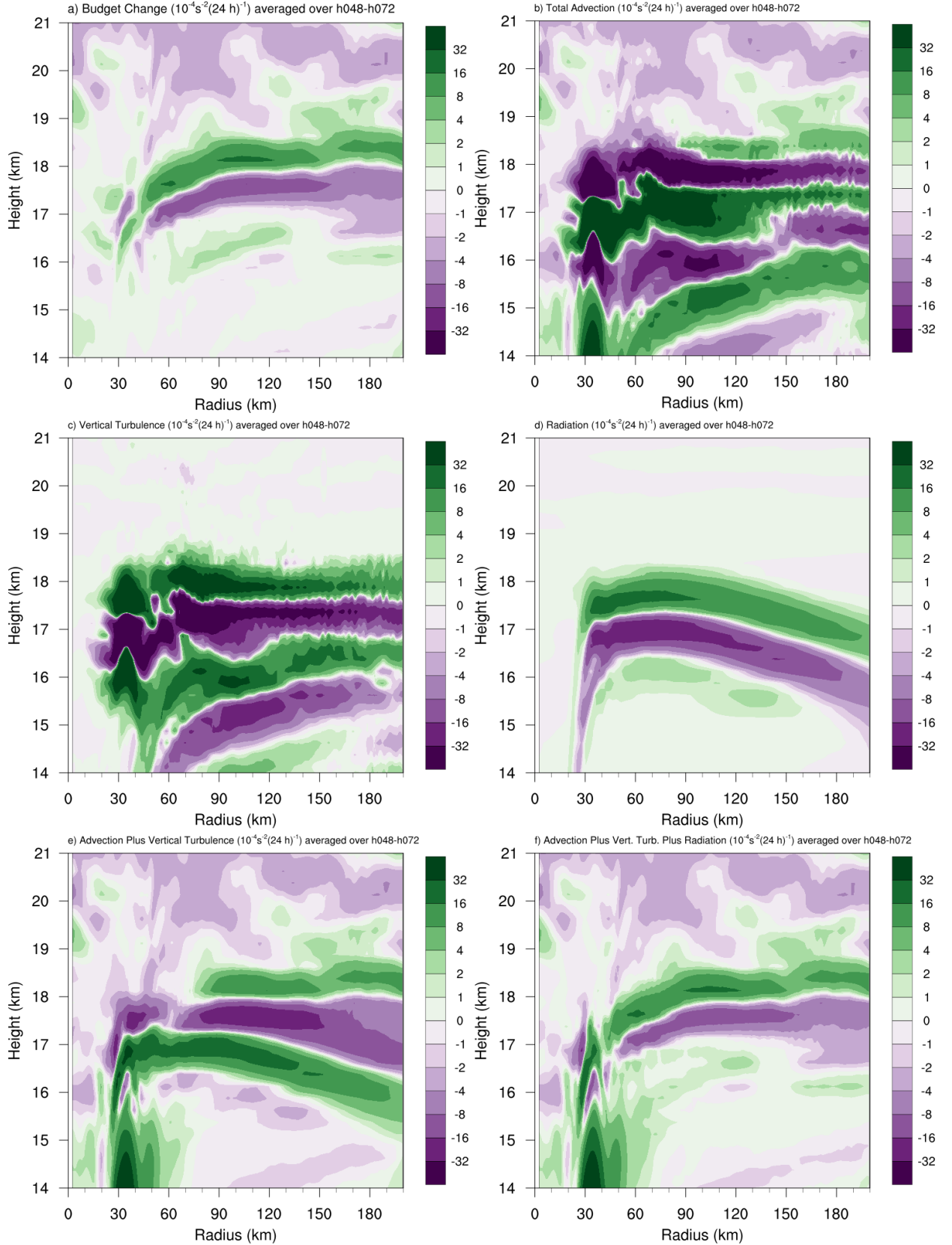


FIG. 7. As in Fig. 5, but for the 48-72-hour period.

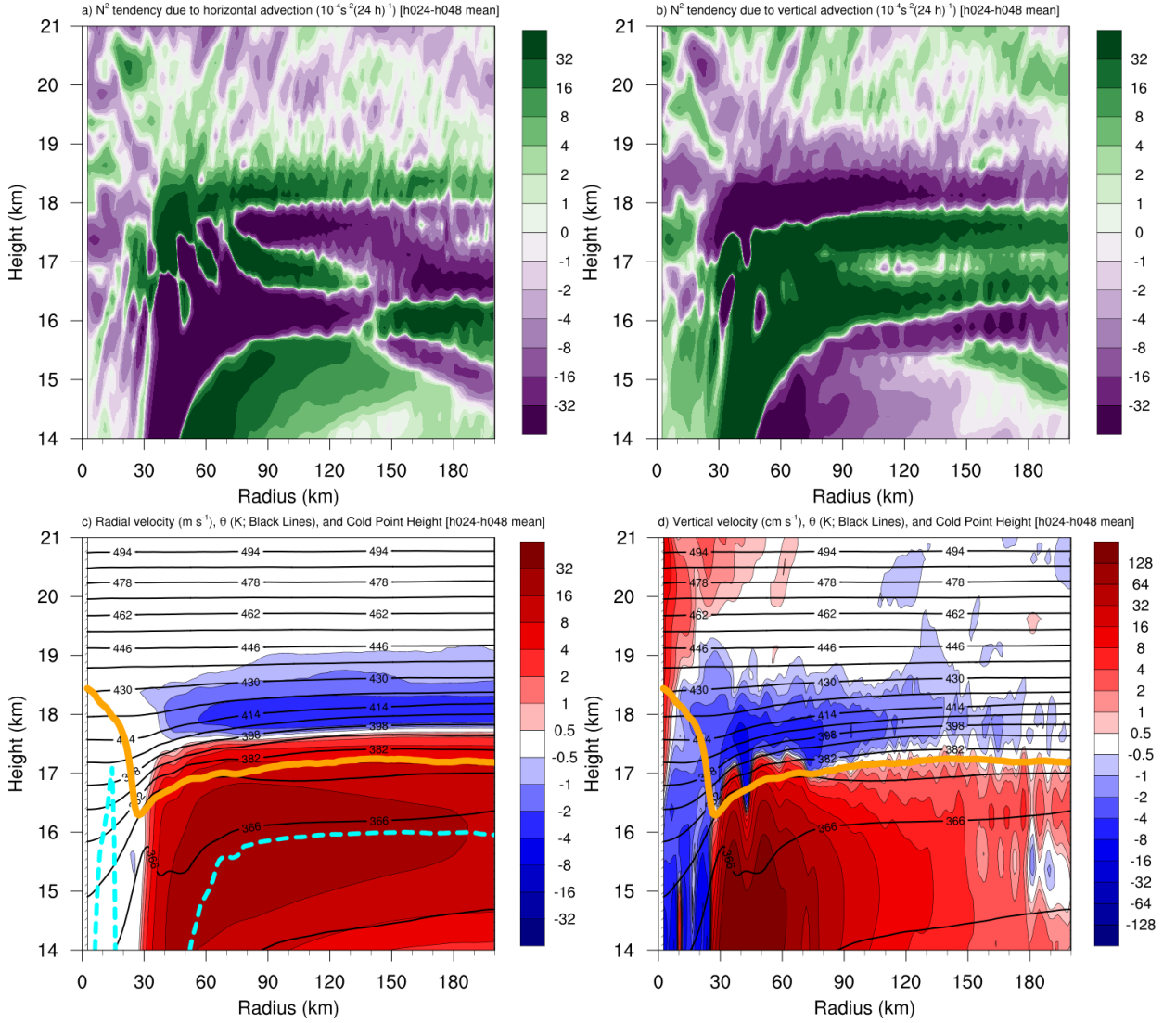
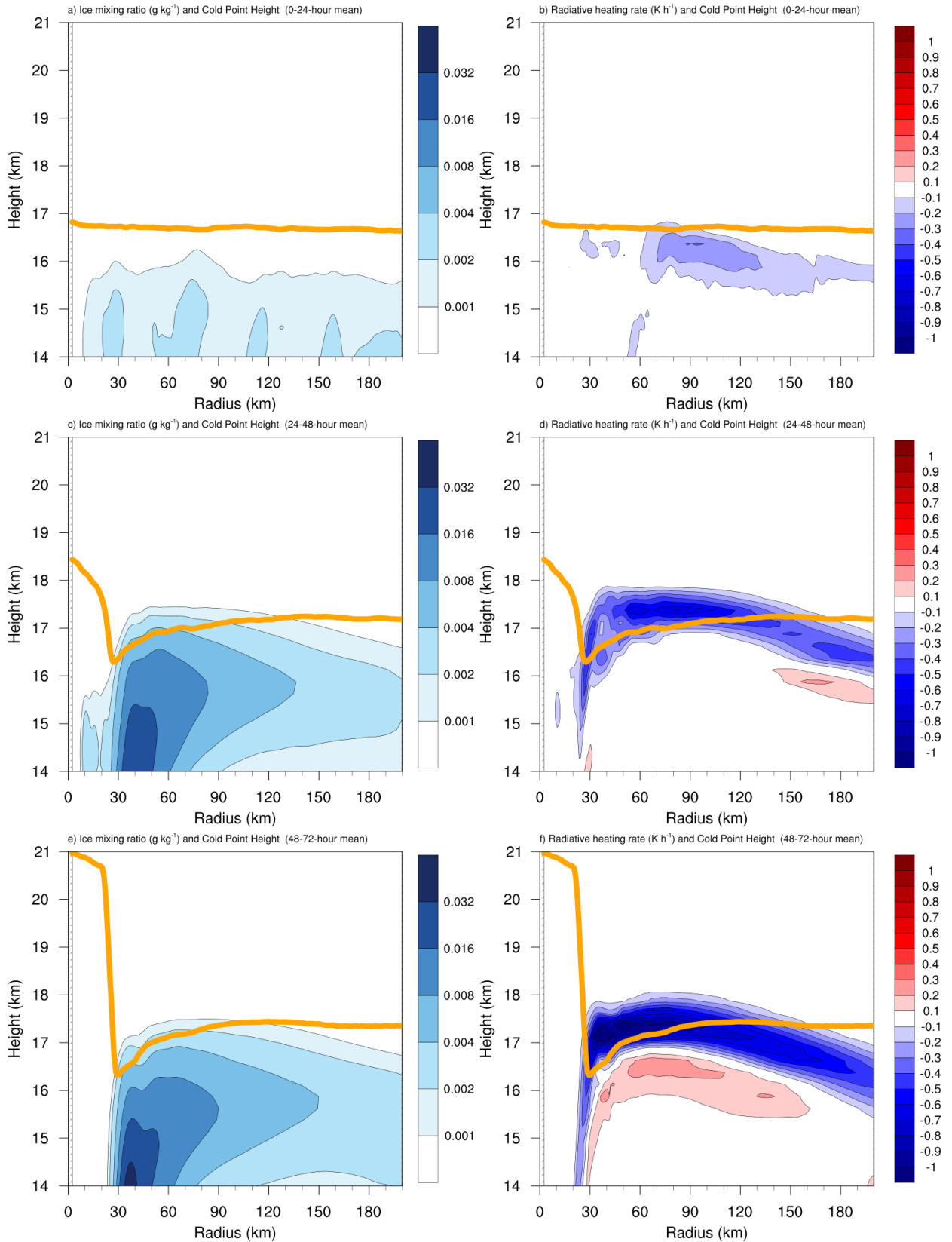


FIG. 8. The contributions to the change in N^2 over the 24-48-hour period ($10^{-4} \text{ s}^{-2} (24 \text{ h})^{-1}$) by (a) horizontal advection and (b) vertical advection. (c) The radial velocity (m s^{-1} ; filled contours), potential temperature (K; thick black contours), cold-point tropopause height (orange line), and level of maximum outflow (dashed cyan line) averaged over the 24-48-hour period. (d) The vertical velocity (cm s^{-1} ; filled contours), potential temperature (K; thick black contours), and cold-point tropopause height (orange line) averaged over the 24-48-hour period.



496 FIG. 9. Ice mixing ratio (g kg^{-1}) and cold-point tropopause height (orange lines) averaged over (a) 0-24 hours,
497 (c) 24-48 hours, and (e) 48-72 hours. Radiative heating rate (K h^{-1}) and cold-point tropopause height (orange
498 lines) averaged over (b) 0-24 hours, (d) 24-48 hours, and (f) 48-72 hours.

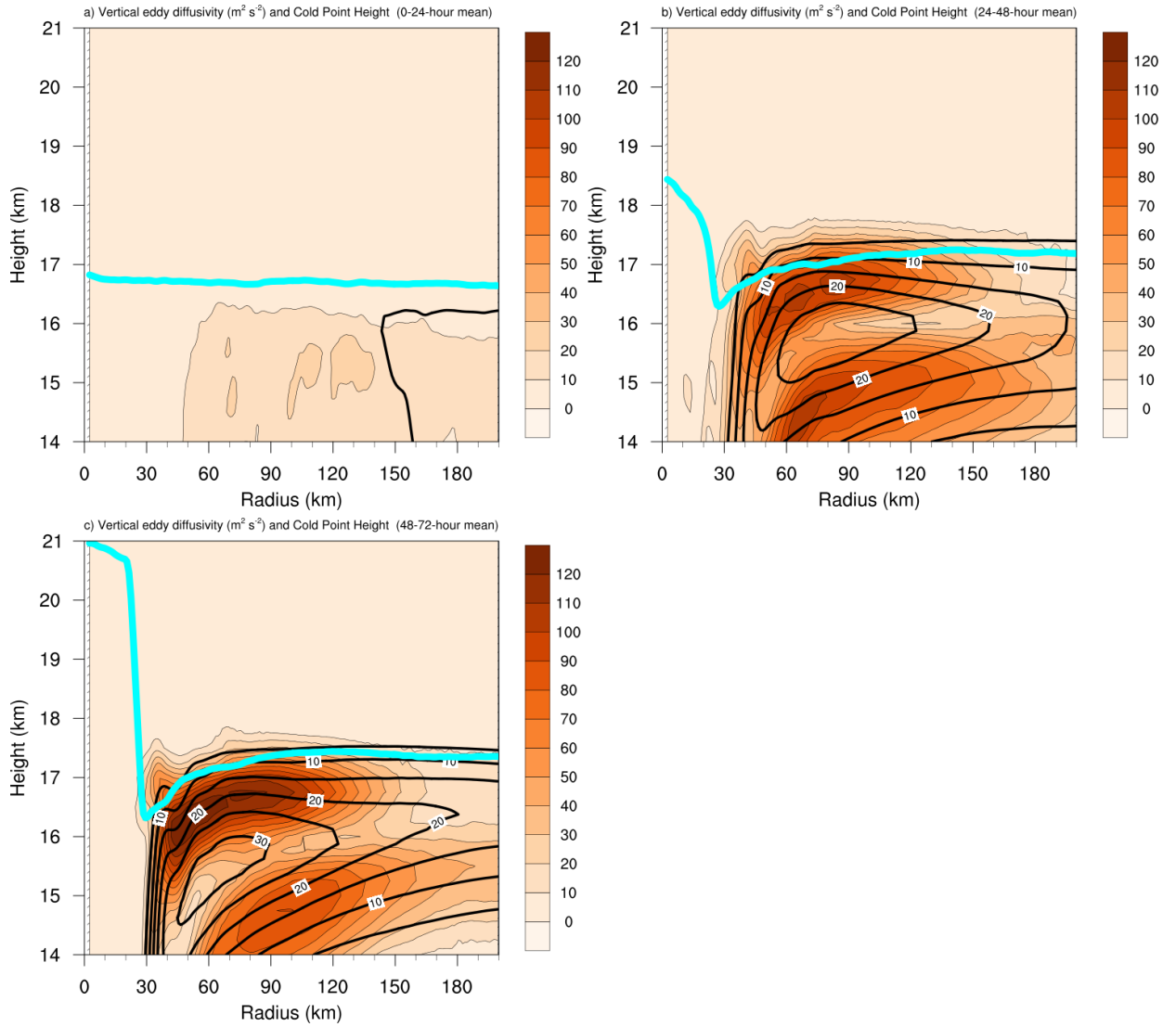
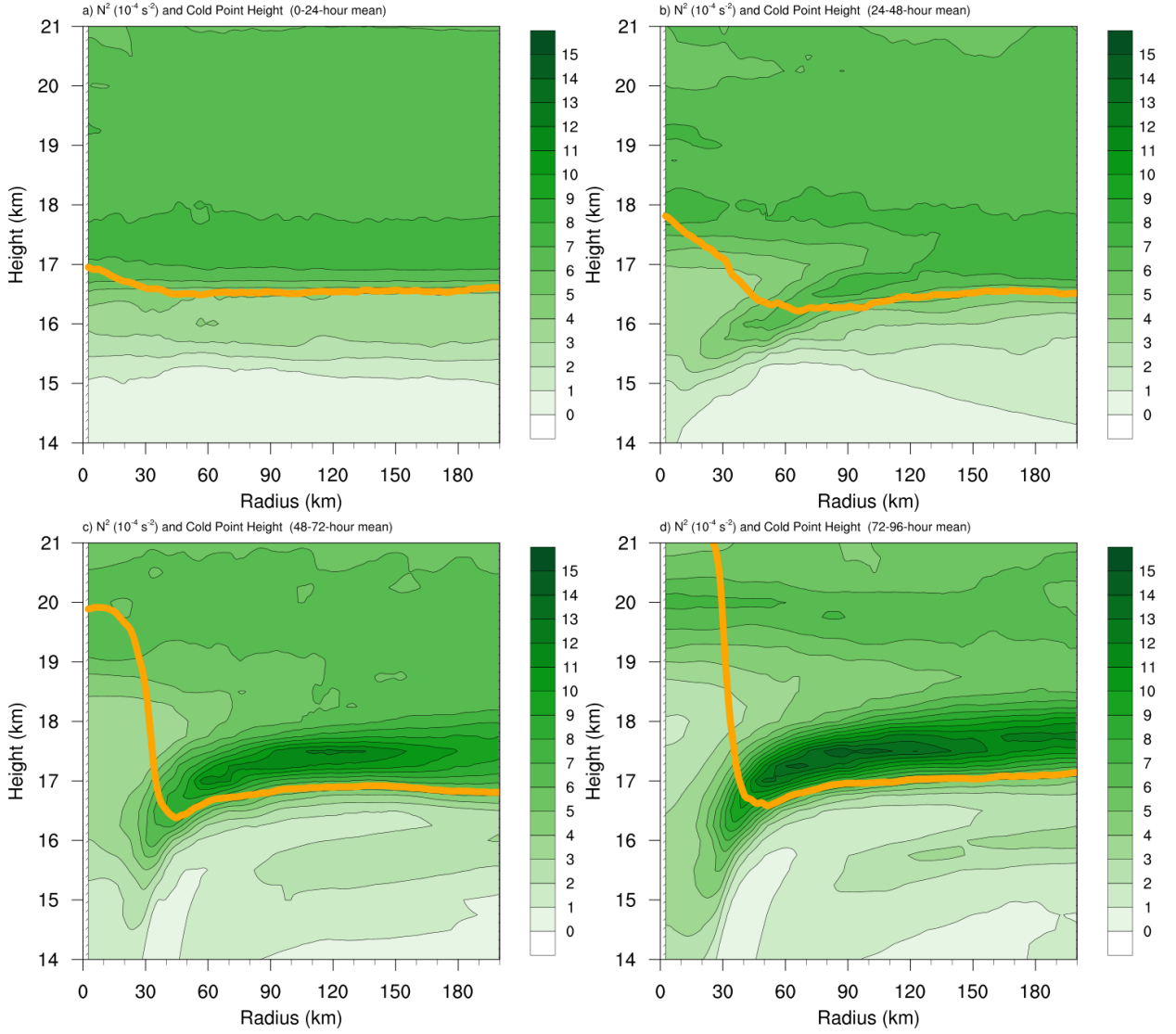


FIG. 10. Vertical eddy diffusivity ($\text{m}^2 \text{s}^{-2}$; filled contours), cold-point tropopause height (cyan lines), and radial velocity (m s^{-1} ; thick black lines) averaged over (a) 0-24 hours, (b) 24-48 hours, and (c) 48-72 hours.



501 Fig. A1. Twenty-four-hour averages of squared Brunt-Väisälä frequency (N^2 ; 10^{-4} s^{-2}) over (a) 0-24 hours,
 502 (b) 24-48 hours, (c) 48-72 hours, and (d) 72-96 hours for the simulation described in Appendix Aa. Orange lines
 503 represent the cold-point tropopause averaged over the same time periods.

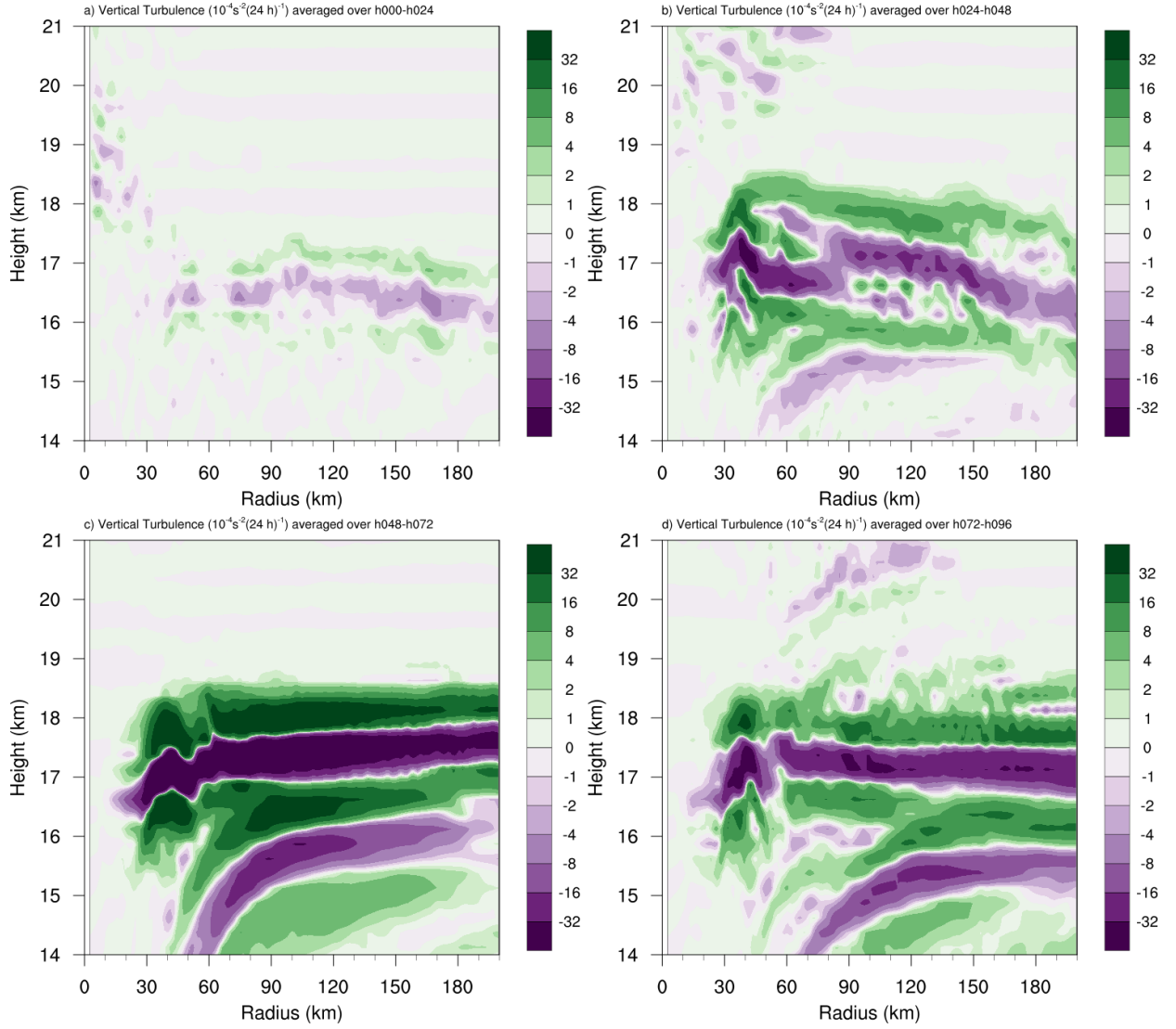


Fig. A2. The contribution of vertical turbulence to the N^2 variability ($10^{-4} \text{s}^{-2} (24 \text{ h})^{-1}$) averaged over (a) 0-24 hours, (b) 24-48 hours, (c) 48-72 hours, and (d) 72-96 hours for the simulation described in Appendix Ab.